

Supplemental information

Modular basis for potent SARS-CoV-2

neutralization by a prevalent

VH1-2-derived antibody class

Micah Rapp, Yicheng Guo, Eswar R. Reddem, Jian Yu, Lihong Liu, Pengfei Wang, Gabriele Cerutti, Phinikoula Katsamba, Jude S. Bimela, Fabiana A. Bahna, Seetha M. Mannepalli, Baoshan Zhang, Peter D. Kwong, Yaoxing Huang, David D. Ho, Lawrence Shapiro, and Zizhang Sheng

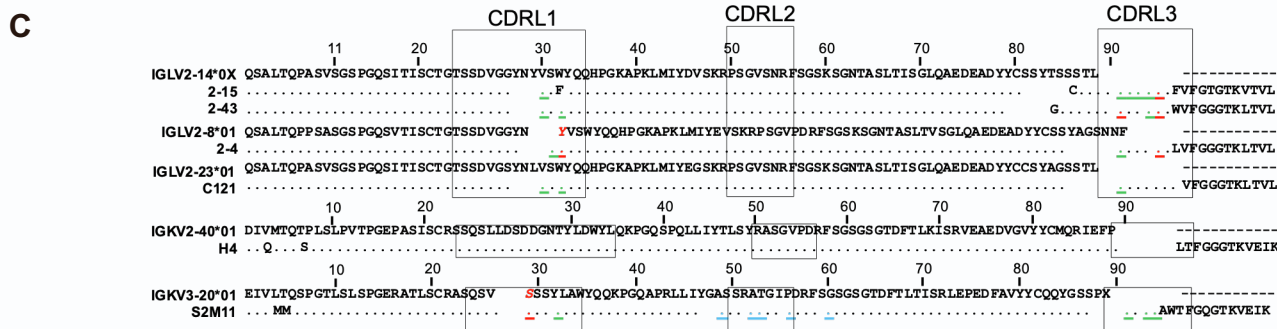
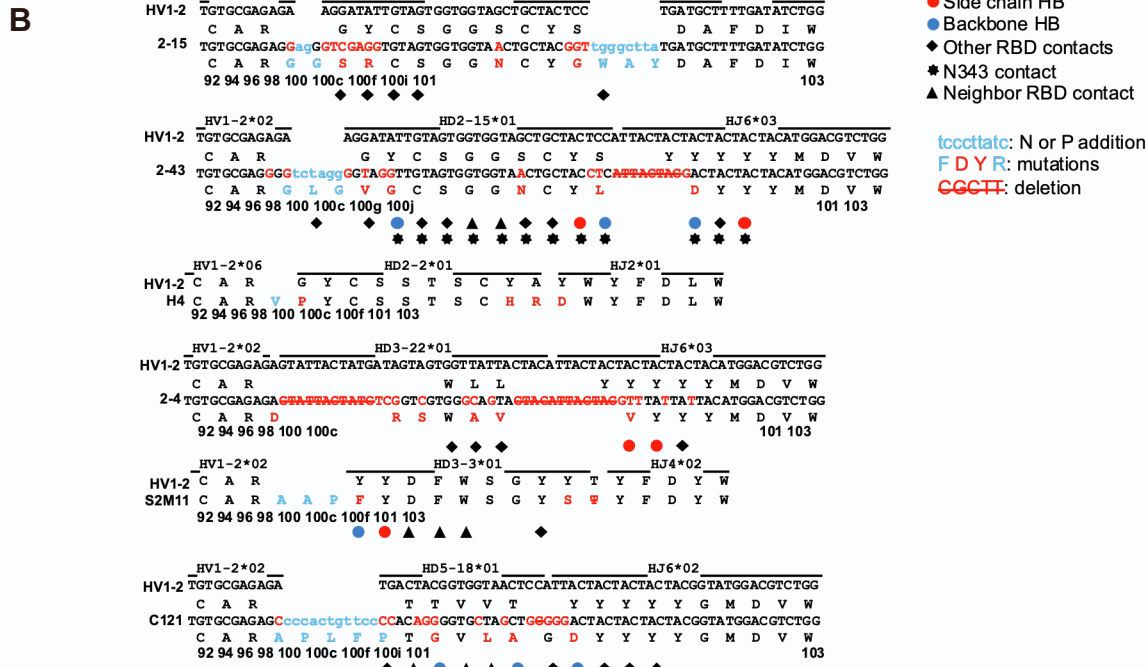
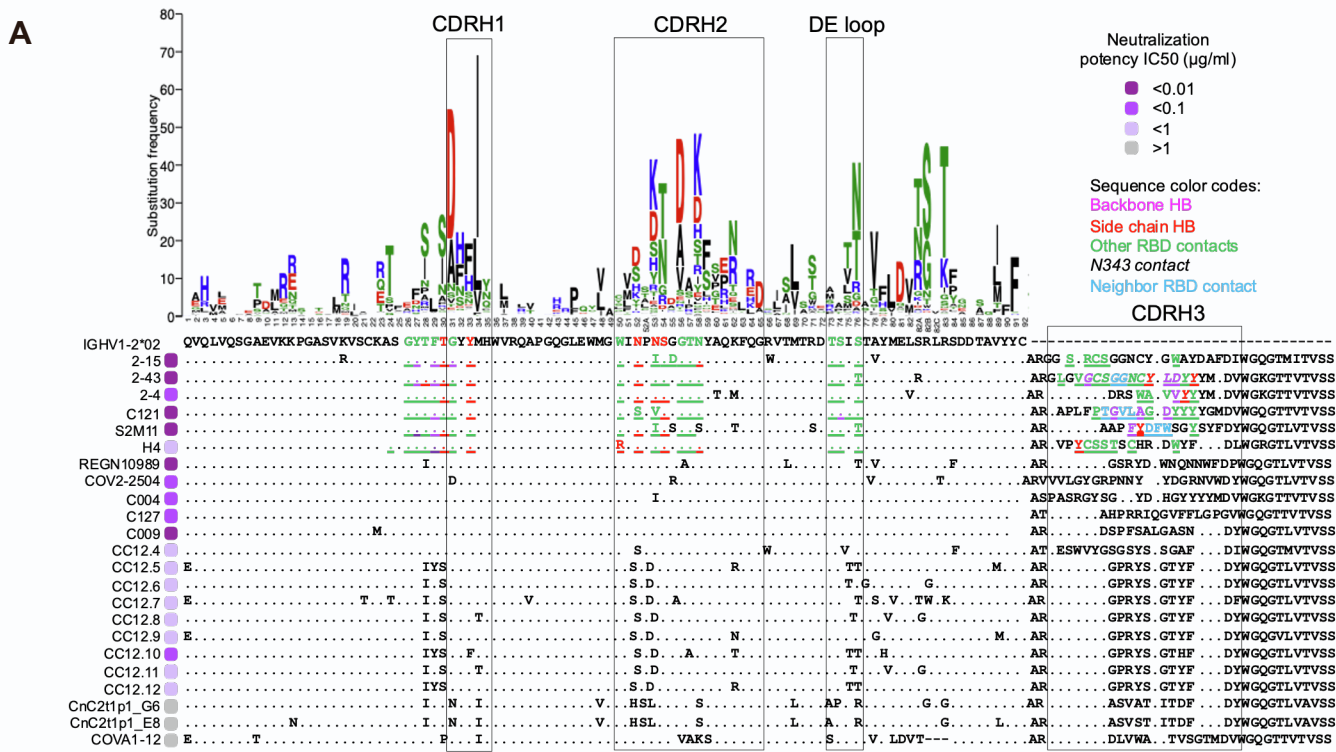


Figure S1. Alignment of heavy and light chain sequences of IGHV1-2 antibodies. Related to Figures 1, 3, 4, 5.
 (A) Heavy chain sequence alignment of the VH1-2-derived antibodies with paratope residues of the VH1-2 class highlighted with underscore. Residues forming backbone hydrogen bonds, side chain hydrogen bond, hydrophobic contact with the SARS-CoV-2 RBD are colored magenta, red, green respectively. Residues contacting quaternary epitopes are colored cyan. Residues interacting with N343 glycan is shown with italic font. Antibody positions and CDR definitions are assigned using the Kabat scheme. The gene-specific substitution profile of VH1-2 gene shows the frequencies of somatic hypermutation to be generated by the somatic hypermutation machinery.
 (B) Heavy chain gene recombination of the six VH1-2 antibodies. For H4 and S2M11, no N- or P-addition sites were determined because the nucleotide sequences are unavailable. H4 paratope residues were not identified due to low resolution of the structure.
 (C) Light chain sequence alignment of the VH1-2 antibody class members with paratope residues highlighted with underscore.

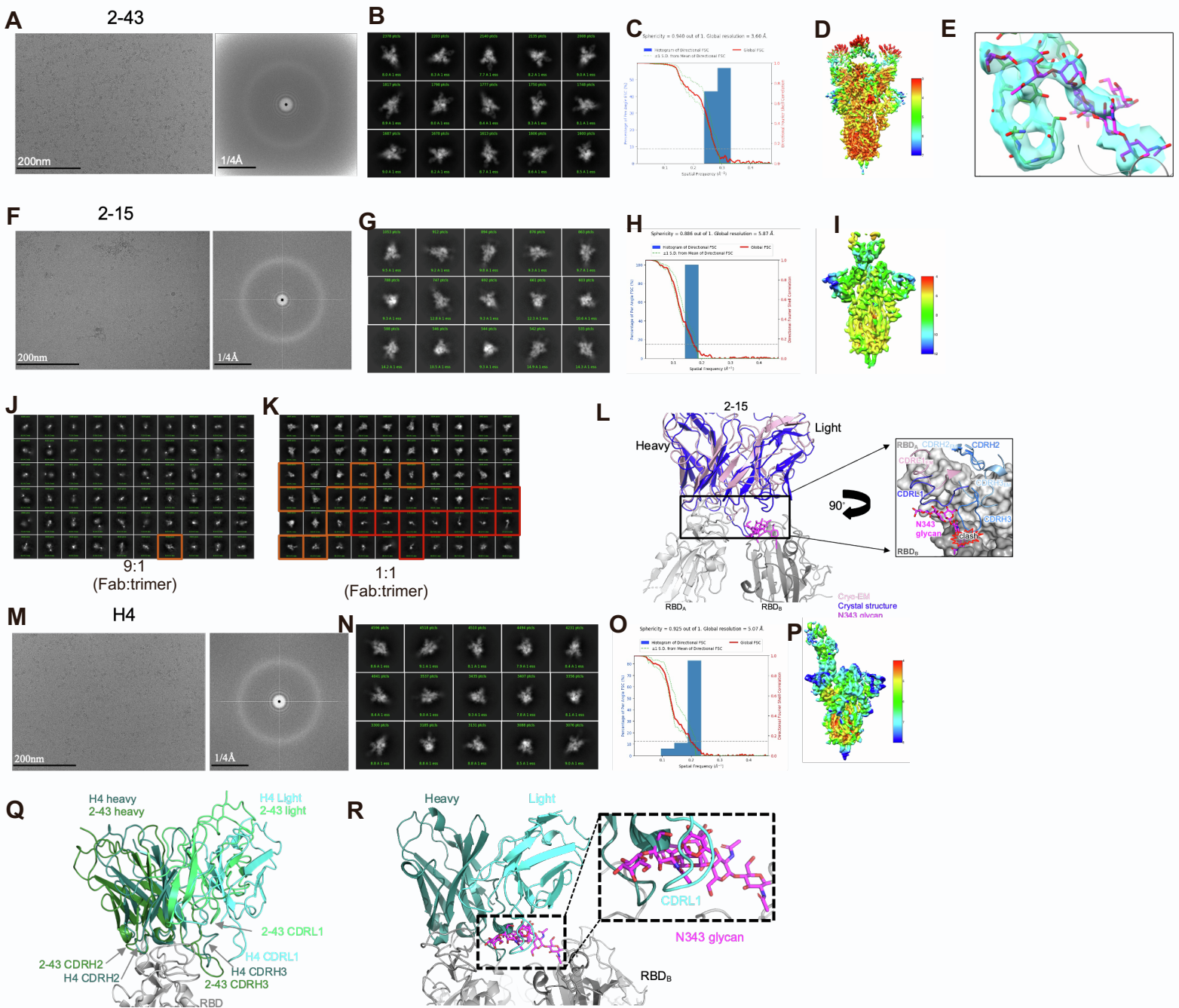


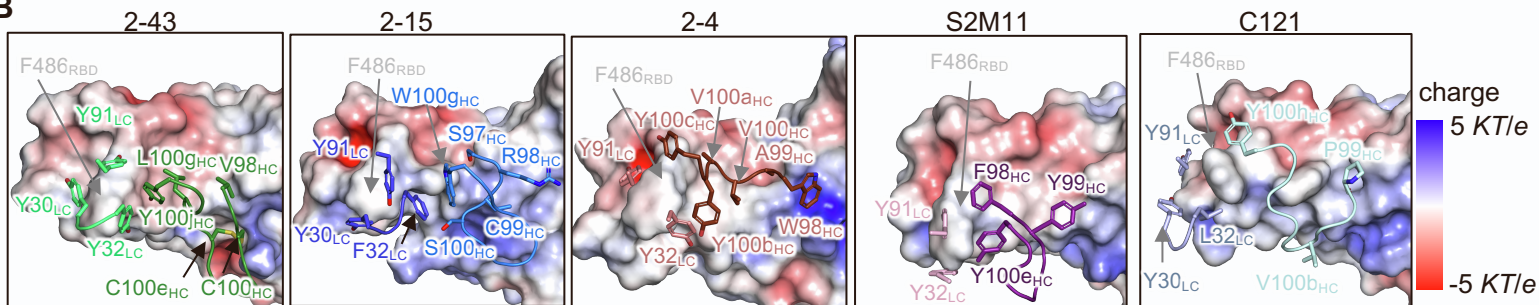
Figure S2. Cryo-EM data processing for antibody 2-43, 2-15, and H4 in complex with the S2P trimer. Related to Figures 2,3, and 4.

- (A) Representative micrograph and CTF of the micrograph of 2-43 complexed with S trimer.
- (B) Representative 2D class averages of 2-43/S complex.
- (C) Resolution of the consensus map of 2-43 /S complex with C3 symmetry as calculated by 3DFSC.
- (D) The local resolution of the full map of 2-43 as calculated by cryoSPARC at an FSC cutoff of 0.5. e, Representative density of the Fab 2-43 and RBD interface.
- (E) Interaction of 2-43 CDRH3 with N343 glycan of an adjacent RBD.
- (F) Representative 2-15 micrograph and CTF of the micrograph.
- (G) Representative 2D class averages of 2-15 complexed with S trimer.
- (H) Resolution of Fab 2-15 in complex with S2P trimer.
- (I) The local resolution of the full 2-15 map as calculated by cryoSPARC at an FSC cutoff of 0.5.
- (J) Disassembly of the SARS-CoV-2 spike by Fab 2-15 in a Fab:S trimer ratio of 9:1. Dimeric spike highlighted in orange, monomeric spike highlighted in red.
- (K) Disassembly of the SARS-CoV-2 spike by Fab 2-15 in a Fab:S trimer ratio of 1:1. Dimeric spike highlighted in orange, monomeric spike highlighted in red.
- (L) Superimposition of 2-15 crystal structure to the 2-15 cryo-EM structure.
- (M) Representative micrograph and CTF of the micrograph of H4 complexed with S trimer.
- (N) Representative H4 2D class averages.
- (O) Resolution of Fab H4 in complex with S trimer.
- (P) The local resolution of the full H4 map as calculated by cryoSPARC at an FSC cutoff of 0.5.
- (Q) Superimposition of H4 to 2-43/spike complex. The heavy chain of the two antibodies have similar binding mode while the light chain of H4 rotated towards the interface between two RBDs.
- (R) Superimposition of H4 to 2-43/spike complex showed that the long CDRL1 of H4 may clash with N343 glycan from an adjacent RBD.

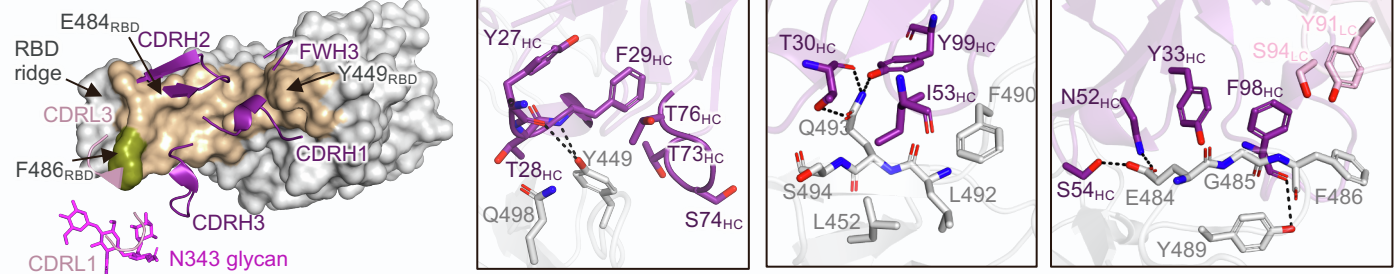
A Buried accessible surface area

	2-43		2-15		H4		2-4		S2M11		C121	
	RBD _A	RBD _B	RBD _A	RBD _B	RBD _A	RBD _B	RBD _A	RBD _B	RBD _A	RBD _B	RBD _A	RBD _B
FWH1	130.5	0	175.51	0	ND	0	129.15	0	122.93	0	112.35	0
CDRH1	18.38	4.18	27.7	0	ND	0	34.52	0	18.04	0	30.96	0
CDRH2	185.45	0	218.53	0	ND	0	266.16	0	191.4	0	161.8	0
FWH3	83.86	0	95.54	0	ND	0	58.68	0	61.74	0	115.52	0
CDRH3	210.06	380.85	194.35	0	ND	0	275.91	44.32	209.02	329.02	259.69	101.23
CDRL1	59.25	51.27	45.62	0	ND	0	34.3	34.43	19.34	110.16	19.84	0
CDRL2	0	14.12	0	0	ND	0	0	0	0	78.13	0	0
CDRL3	68.99	0	64.23	0	ND	0	93.07	0	35	0	39.54	0
Total paratope	625.99	450.42	645.97	0	ND	0	762.64	78.75	534.54	517.31	627.35	101.23
Total epitope	812.92	548.57	810.44	0	ND	0	785.72	74.9	671.75	469.65	822.12	73.56
Total	1438.9	998.99	1456.4	0	ND	0	1548.4	153.65	1206.3	986.96	1449.5	174.79

B



C S2M11



D C121

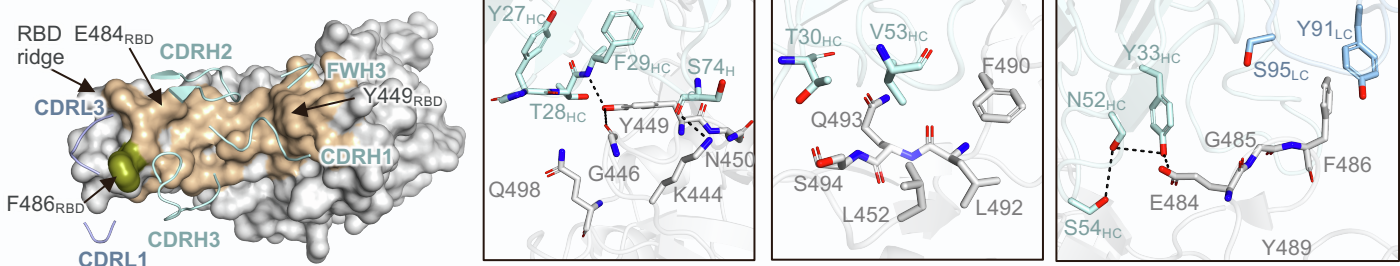


Figure S3. Paratope-epitope interactions of the VH1-2 antibody class. Related to figures 3, 4, 5, and 6.

- (A) Buried accessible surface areas at paratope and epitope interfaces. Note: RBD_A is the RBD protomer with receptor binding motif recognized by antibody while RBD_B is the RBD protomer providing quaternary epitope.
- (B) Hydrophobic interactions between antibody CDRH3, CDRL1, and CDRL3 and RBD. The RBD is colored with electrostatic potential. Side chains are shown for residues with buried accessible surface area more than 20 Å².
- (C) Overview of the S2M11 epitope (left panel) and close-up view of the hydrogen bond networks between S2M11 and the SARS-CoV-2 RBD (right three panels). The RBD epitope recognized by S2M11 heavy and light chains are colored wheat and orange respectively (RBD_A, light gray). Epitope residues interacting with both heavy and light chains were colored lemon. S2M11 also binds to N343 glycan (magenta) from a neighboring RBD (RBD_B, dark gray). Hydrogen bonds are shown as black dashed lines. PDB structure 7K43 is used.
- (D) Overview of the C121 epitope (left panel) and close-up view of the hydrogen bond networks between C121 and the SARS-CoV-2 RBD (right three panels) (PDB ID 7K8X). The RBD epitope recognized by C121 heavy (palecyan) and light (lightblue) chains are colored wheat and orange respectively (RBD_A, light gray). Epitope residues interacting with both heavy and light chains are colored lemon.

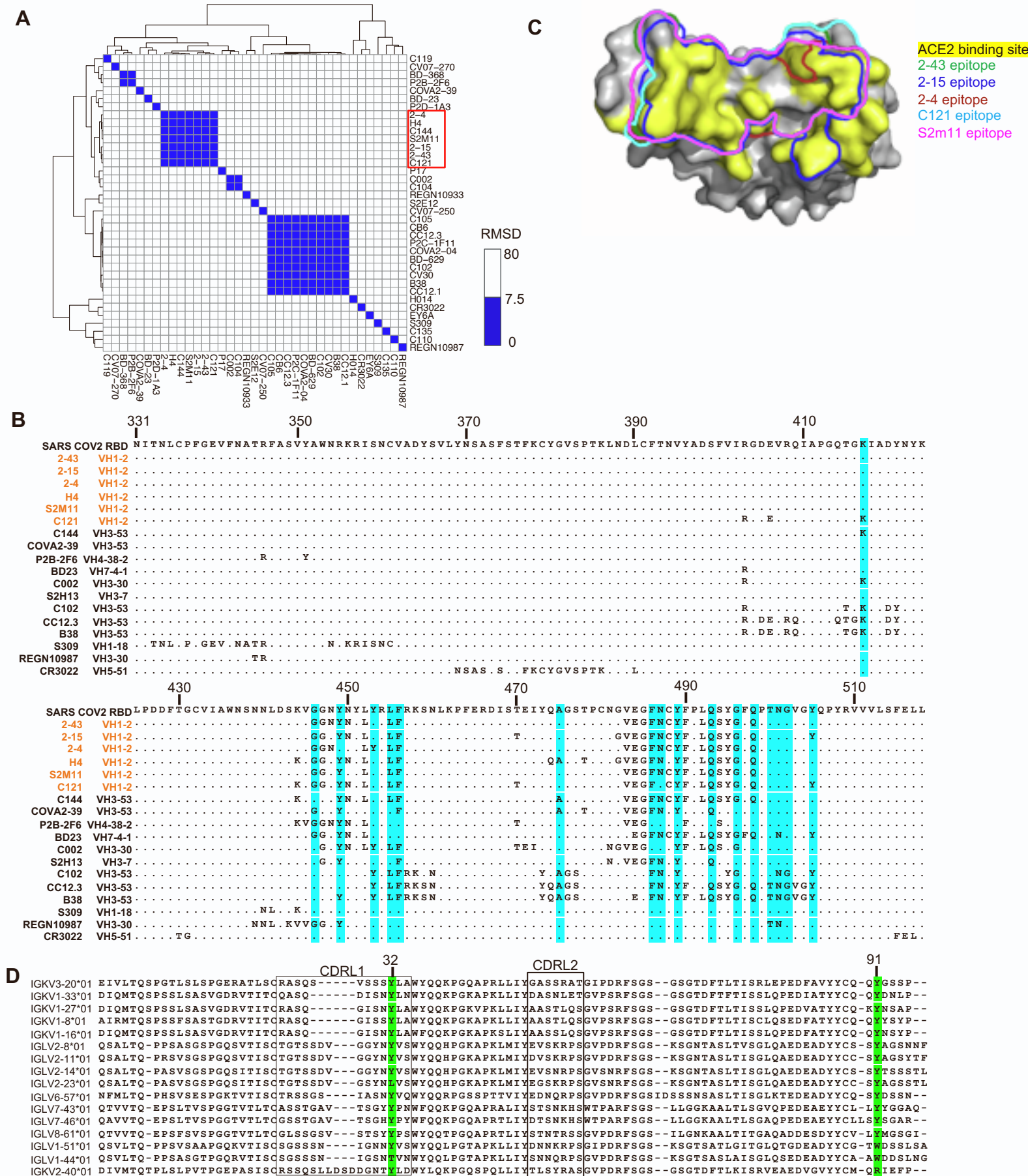


Figure S4. Similarities in binding orientation and epitopes of RBD-targeting antibodies. Related to figure 4.

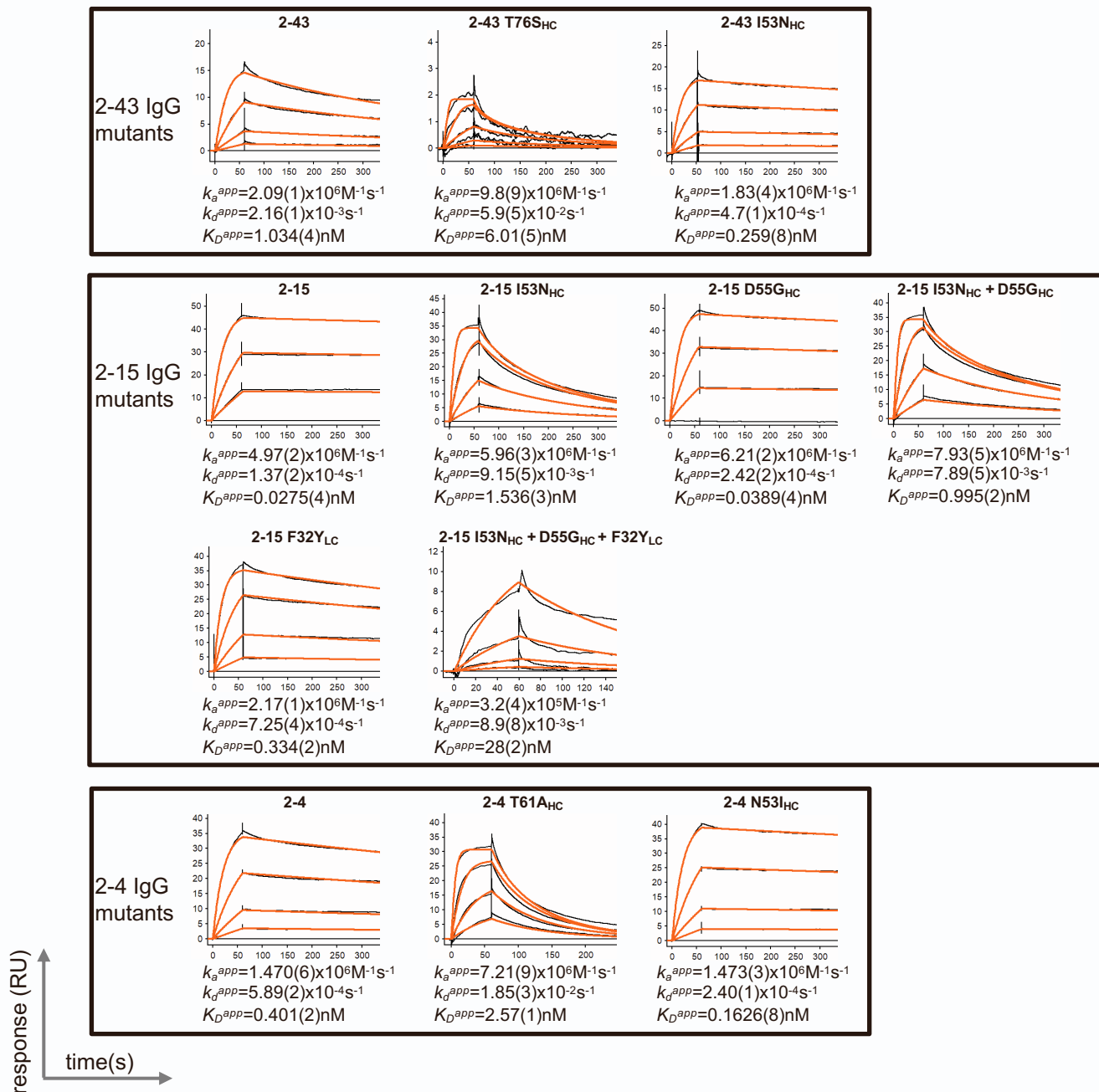
(A) Clustering of SARS-CoV-2 RBD-targeting antibodies. For each pair of antibodies, the RBDs were superimposed and the RMSD of Ca atom between antibody variable domains were then calculated. Antibodies were then clustered using the calculated pairwise RMSD values.

(B) Epitope residues of SARS-CoV-2 RBD-targeting antibodies. For each antibody, epitope residues are shown and non-epitope residues are masked with dots. ACE2 binding site residues are highlighted with cyan background.

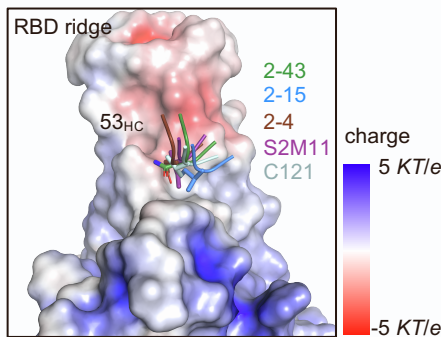
(C) The VH1-2 class antibodies have RBD epitopes that overlap with the ACE2 binding site.

(D) Alignment of the light chain germline genes used by the SARS-CoV-2 RBD-targeting VH1-2 antibodies in Figure 1C as well as other germline genes having residues Y32_{LC} and Y91_{LC}.

A



B



C

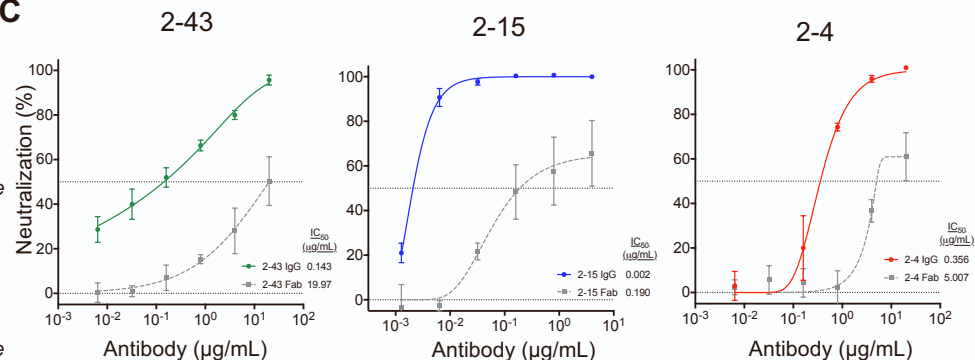


Figure S5. Apparent IgG binding affinity profiles, interaction of 53_{HC} with RBD, and avidity effects of the VH1-2 antibodies. Related to figure 5.

(A) Surface plasmon resonance profiles of 2-43, 2-15, and 2-4 antibody variants. The black traces represent the experimental data, and the red traces represent the fit to an 1:1 interaction model. The number in brackets represents the error of the fit in the last integer.

(B) Interaction of 53_{HC} side chain with a hydrophobic pocket in RBD. RBD from 2-15/RBD complex is shown in surface mode and colored by electrostatic potential. APBS in PyMOL was used to calculate electrostatics.

(C) Pseudovirus neutralization profiles of Fabs 2-43, 2-15, and 2-4 showed significantly lower potency than IgG, suggesting avidity effect is important for achieving high neutralization potency. Data represent mean \pm SEM of technical triplicates.

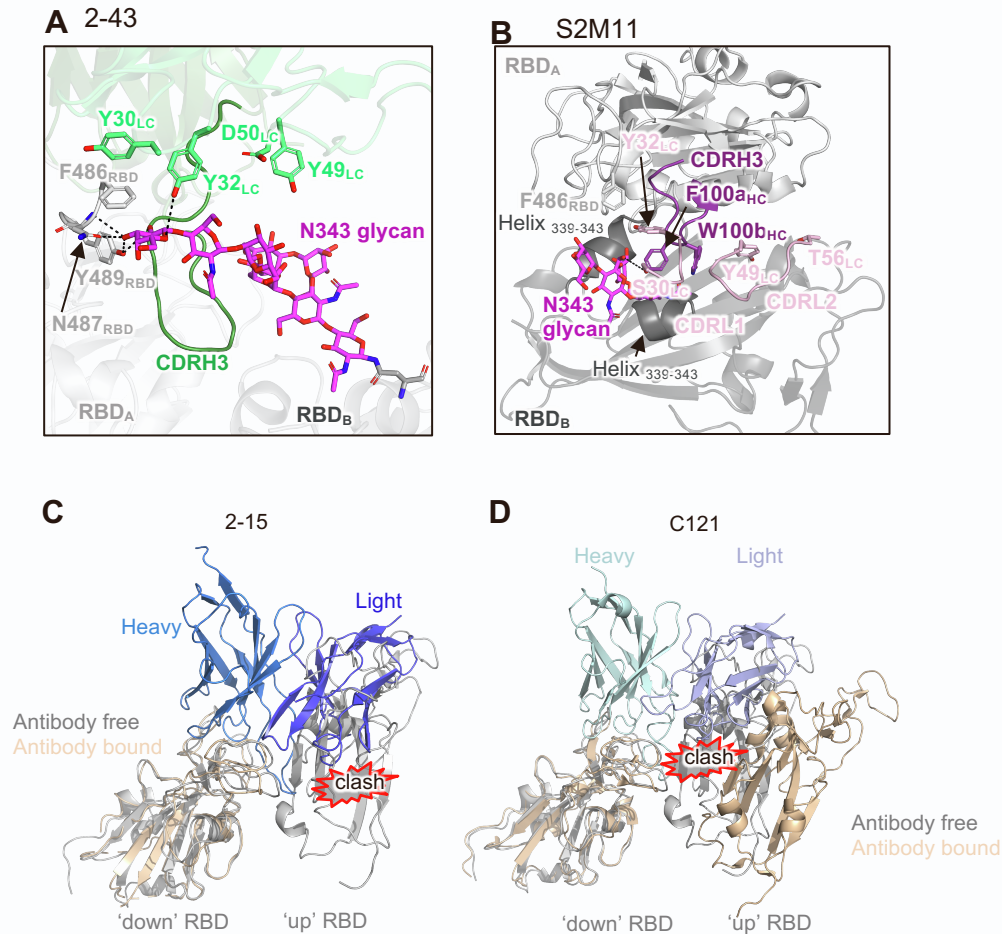


Figure S6. Quaternary recognition of 2-4 and S2M11 and potential interactions of 2-15, and C121 with adjacent ‘up’ RBDs. Related to Figure 6.

(A) The CDRL1 and CDRL2 (green) of 2-43 and RBD interact with one branch of the N343 glycan (magenta) from the adjacent RBD (RBD_B). The side chain of D50_{LC} was modeled in PyMOL. N343 glycan also interacts with the RBD ridge in RBD_A.

(B) Close-up view of the S2M11 quaternary epitope between two RBDs mediated by CDRH3, CDRL1, and CDRL2.

(C) Superimposition of 2-15 in complex with RBD to antibody-free SARS-CoV-2 spike (PDBID: 6zgg). The light chain of 2-15 clashes with the adjacent ‘up’ RBD from the antibody free spike.

(D) Superimposition of C121 in complex with spike to antibody-free SARS-CoV-2 spike. The distance between the two RBD protomers increases in C121 bound spike, suggesting that the interaction of C121 light chain with the adjacent ‘up’ RBD induces conformation change in RBDs.

Table S1. SARS-CoV-2 neutralizing antibodies identified from infected humans. Related to Figure 1.

Antibody	IGHV	IGHJ	IGLV	IGLJ	Pseudovirus neutralization (IC ₅₀ , µg/mL)	live virus neutralization (IC ₅₀ , µg/mL)	Reference
1-20	IGHV3-53	IGHJ6	IGKV1-9	IGKJ3	0.127	0.008	Liu et al. 2020
1-57	IGHV3-72	IGHJ4	IGKV3-20	IGKJ2	0.009	0.008	Liu et al. 2020
1-68	IGHV1-24	IGHJ6	IGLV2-18*02	IGLJ1	0.767	0.014	Liu et al. 2020
1-87	IGHV1-24	IGHJ6	IGLV2-14	IGLJ1	0.095	0.086	Liu et al. 2020
2-15	IGHV1-2	IGHJ3	IGLV2-14	IGLJ1	0.005	0.001	Liu et al. 2020
2-17	IGHV1-69	IGHJ5	IGKV3-15	IGKJ4	0.168	0.007	Liu et al. 2020
2-30	IGHV3-30	IGHJ6	IGKV1-9	IGKJ4	0.512	0.050	Liu et al. 2020
2-36	IGHV4-61	IGHJ3	IGKV3-20	IGKJ1	0.044	0.209	Liu et al. 2020
2-38	IGHV3-21	IGHJ3	IGLV3-19	IGLJ3	0.232	0.208	Liu et al. 2020
2-4	IGHV1-2	IGHJ6	IGLV2-8	IGLJ3	0.394	0.057	Liu et al. 2020
2-43	IGHV1-2	IGHJ6	IGLV2-14	IGLJ3	0.071	0.003	Liu et al. 2020
2-51	IGHV1-24	IGHJ4	IGLV2-8	IGLJ3	0.652	0.007	Liu et al. 2020
2-7	IGHV2-5	IGHJ4	IGLV2-14	IGLJ3	0.010	0.003	Liu et al. 2020
4-18	IGHV3-30	IGHJ5	IGLV3-25	IGLJ3	0.023	0.020	Liu et al. 2020
4-19	IGHV4-59	IGHJ6	IGKV1-9	IGKJ4	0.070	0.109	Liu et al. 2020
4-20	IGHV1-46	IGHJ4	IGKV1-39	IGKJ1	0.036	0.017	Liu et al. 2020
4-8	IGHV1-69	IGHJ6	IGLV3-1	IGLJ3	0.032	0.009	Liu et al. 2020
5-24	IGHV3-33	IGHJ6	IGKV3-20	IGKJ4	0.013	0.008	Liu et al. 2020
5-7	IGHV1-46	IGHJ6	IGKV1-9	IGKJ3	0.050	0.033	Liu et al. 2020
B38	VH3-53/66	IGHJ6	IGKV1-9	IGKJ2	-	0.177	Wu et al., 2020
B5	VH1-2	IGHJ6	IGKV3-20	IGKJ1	-	1.375	Wu et al., 2020
H2	IGHV3-9	IGHJ5	IGKV1-39	IGKJ4	-	1.000	Wu et al., 2020
H4	VH1-2	IGHJ2	IGKV2-40	IGKJ2	-	0.896	Wu et al., 2020
C002	IGHV3-30	IGHJ4	IGKV1-39	IGKJ1	0.009	-	Robbiani et al., 2020
C003	IGHV3-53	IGHJ4	IGKV3-20	IGKJ2	0.314	-	Robbiani et al., 2020
C004	IGHV1-2	IGHJ6	IGKV1-33	IGKJ5	0.011	-	Robbiani et al., 2020
C005	IGHV1-58	IGHJ3	IGKV3-20	IGKJ1	0.060	-	Robbiani et al., 2020
C006	IGHV3-11	IGHJ6	IGLV1-44	IGLJ3	0.322	-	Robbiani et al., 2020
C008	IGHV3-30	IGHJ4	IGKV1-5	IGKJ1	0.625	-	Robbiani et al., 2020
C009	IGHV1-2	IGHJ4	IGLV2-8	IGLJ3	0.005	-	Robbiani et al., 2020
C013	IGHV1-69	IGHJ6	IGKV3-11	IGKJ4	0.042	-	Robbiani et al., 2020
C017	IGHV3-9	IGHJ5	IGKV3-11	NA	0.073	-	Robbiani et al., 2020
C022	IGHV4-39	IGHJ1	IGKV1-5	IGKJ2	0.074	-	Robbiani et al., 2020
C037	IGHV1-58	IGHJ3	IGKV3-20	IGKJ1	0.156	-	Robbiani et al., 2020
C101	IGHV3-53	IGHJ4	IGKV3-20	IGKJ1	0.008	-	Robbiani et al., 2020
C102	IGHV3-53	IGHJ4	IGKV3-20	IGKJ1	0.034	-	Robbiani et al., 2020
C103	IGHV4-34	IGHJ3	IGKV3-20	IGKJ4	0.004	-	Robbiani et al., 2020
C104	IGHV4-34	IGHJ3	IGKV3-20	IGKJ4	0.023	-	Robbiani et al., 2020
C105	IGHV3-53	IGHJ4	IGLV2-8	IGLJ3	0.026	-	Robbiani et al., 2020
C108	IGHV4-4	IGHJ3	IGLV2-14	IGLJ1	0.481	-	Robbiani et al., 2020
C110	IGHV5-51	IGHJ3	IGKV1-5	IGKJ2	0.018	-	Robbiani et al., 2020
C112	IGHV3-30	IGHJ4	IGLV2-14	IGLJ3	0.112	-	Robbiani et al., 2020
C115	IGHV3-49	IGHJ4	IGKV2-28	IGKJ2	0.198	-	Robbiani et al., 2020
C117	IGHV3-30	IGHJ4	IGLV1-51	IGLJ1	0.348	-	Robbiani et al., 2020
C118	IGHV3-30	IGHJ6	IGLV4-69	IGLJ3	0.104	-	Robbiani et al., 2020
C119	IGHV1-46	IGHJ6	IGLV2-14	IGLJ3	0.009	-	Robbiani et al., 2020
C120	IGHV3-53	IGHJ5	IGKV1-33	IGKJ4	0.013	-	Robbiani et al., 2020
C121	IGHV1-2	IGHJ6	IGLV2-23	IGLJ3	0.007	0.002	Robbiani et al., 2020
C122	IGHV3-53	IGHJ4	IGKV1-9	IGKJ2	0.023	-	Robbiani et al., 2020
C123	IGHV3-53	IGHJ3	IGKV1-9	IGKJ5	0.149	-	Robbiani et al., 2020
C124	IGHV3-48	IGHJ4	IGKV3-11	IGKJ1	0.342	-	Robbiani et al., 2020
C125	IGHV1-58	IGHJ3	IGKV3-20	IGKJ1	0.043	-	Robbiani et al., 2020

Table S1. Continued

C127	IGHV1-2	IGHJ6	IGLV1-44	IGLJ3	0.069	-	Robbiani et al., 2020
C128	IGHV3-23	IGHJ6	IGKV3-20	IGKJ4	0.101	-	Robbiani et al., 2020
C129	IGHV3-30	IGHJ3	IGKV1-33	IGKJ5	0.011	-	Robbiani et al., 2020
C131	IGHV1-69	IGHJ6	IGKV3-15	IGKJ5	0.031	-	Robbiani et al., 2020
C132	IGHV4-4	IGHJ4	IGLV2-14	IGLJ3	0.709	-	Robbiani et al., 2020
C135	IGHV3-30	IGHJ4	IGKV1-5	IGKJ1	0.017	0.003	Robbiani et al., 2020
C140	IGHV3-66	IGHJ6	IGKV1-9	IGKJ2	0.024	-	Robbiani et al., 2020
C144	IGHV3-53	IGHJ4	IGLV2-14	IGLJ1	0.007	0.003	Robbiani et al., 2020
C145	IGHV3-53	IGHJ4	IGLV2-14	IGLJ1	0.003	-	Robbiani et al., 2020
C149	IGHV3-30	IGHJ4	IGKV1-39	IGKJ4	0.045	-	Robbiani et al., 2020
C151	IGHV3-21	IGHJ5	IGLV6-57	IGLJ3	0.032	-	Robbiani et al., 2020
C152	IGHV1-18	IGHJ6	IGKV1-27	IGKJ1	0.022	-	Robbiani et al., 2020
C153	IGHV3-53	IGHJ4	IGLV2-23	IGLJ3	0.071	-	Robbiani et al., 2020
C154	IGHV3-30	IGHJ4	IGKV1-33	IGKJ5	0.436	-	Robbiani et al., 2020
C155	IGHV3-53	IGHJ4	IGKV3-15	IGKJ1	0.011	-	Robbiani et al., 2020
C161	IGHV4-34	IGHJ3	IGKV3-20	IGKJ4	0.042	-	Robbiani et al., 2020
C162	IGHV4-34	IGHJ3	IGKV3-20	IGKJ4	0.014	-	Robbiani et al., 2020
C163	IGHV4-34	IGHJ3	IGKV3-20	IGKJ4	0.010	-	Robbiani et al., 2020
C164	IGHV3-66	IGHJ3	IGLV2-23	IGLJ3	0.239	-	Robbiani et al., 2020
C165	IGHV1-69	IGHJ3	IGKV3-20	IGKJ1	0.041	-	Robbiani et al., 2020
C207	IGHV3-23	IGHJ4	IGKV3-11	IGKJ1	0.159	-	Robbiani et al., 2020
C210	IGHV3-53	IGHJ6	IGKV1-9	IGKJ4	0.051	-	Robbiani et al., 2020
C211	IGHV3-66	IGHJ4	IGKV3-15	IGKJ1	0.013	-	Robbiani et al., 2020
CC12.1	IGHV3-53	IGHJ6	IGKV1-9	IGKJ3	0.019	0.022	Rogers et al., 2020
CC12.10	IGHV1-2	IGHJ4	IGLV2-14	IGLJ3	0.070	0.058	Rogers et al., 2020
CC12.11	IGHV1-2	IGHJ4	IGLV2-14	IGLJ3	0.140	0.160	Rogers et al., 2020
CC12.12	IGHV1-2	IGHJ4	IGLV2-14	IGLJ3	1.500	0.540	Rogers et al., 2020
CC12.13	IGHV3-53	IGHJ4	IGKV1-33	IGKJ5	0.100	0.090	Rogers et al., 2020
CC12.14	IGHV3-21	IGHJ6	IGKV2-30	IGKJ3	0.023	0.089	Rogers et al., 2020
CC12.15	IGHV3-48	IGHJ4	IGLV1-40	IGLJ3	3.700	4.500	Rogers et al., 2020
CC12.16	IGHV3-33	IGHJ4	IGLV3-21	IGLJ3	>50	10.000	Rogers et al., 2020
CC12.17	IGHV3-30	IGHJ6	IGLV3-21	IGLJ3	2.100	8.600	Rogers et al., 2020
CC12.18	IGHV1-46	IGHJ4	IGLV6-57	IGLJ3	16.000	6.300	Rogers et al., 2020
CC12.19	IGHV3-23	IGHJ6	IGLV3-21	IGLJ3	>50	10.000	Rogers et al., 2020
CC12.2	IGHV3-53	IGHJ4	IGKV3-20	IGKJ2	0.220	0.016	Rogers et al., 2020
CC12.23	IGHV4-39	IGHJ4	IGLV3-25	IGLJ3	22.000	8.700	Rogers et al., 2020
CC12.3	IGHV3-53	IGHJ4	IGKV3-20	IGKJ2	0.018	0.026	Rogers et al., 2020
CC12.4	IGHV1-2	IGHJ3	IGLV2-8	IGLJ3	0.110	0.710	Rogers et al., 2020
CC12.5	IGHV1-2	IGHJ4	IGLV2-14	IGLJ3	0.330	0.520	Rogers et al., 2020
CC12.6	IGHV1-2	IGHJ4	IGLV2-14	IGLJ3	0.490	0.290	Rogers et al., 2020
CC12.7	IGHV1-2	IGHJ4	IGLV2-14	IGLJ3	0.260	0.460	Rogers et al., 2020
CC12.8	IGHV1-2	IGHJ4	IGLV2-14	IGLJ3	0.110	0.260	Rogers et al., 2020
CC12.9	IGHV1-2	IGHJ4	IGLV2-14	IGLJ3	23.000	0.610	Rogers et al., 2020
CC6.29	IGHV7-4-1	IGHJ5	IGKV1-39	IGKJ3	0.002	0.007	Rogers et al., 2020
CC6.31	IGHV1-46	IGHJ4	IGKV1-17	IGKJ4	0.059	0.053	Rogers et al., 2020
CC6.32	IGHV3-9	IGHJ4	IGLV3-21	IGLJ6	1.100	3.500	Rogers et al., 2020
COVA1-03	IGHV3-30	IGHJ6	IGKV1-27	IGKJ3	0.420	10.000	Brouwer et al., 2020
COVA1-12	IGHV1-2	IGHJ6	IGLV2-8	IGLJ3	1.300	1.400	Brouwer et al., 2020
COVA1-16	IGHV1-46	IGHJ1	IGKV1-33	IGKJ4	0.130	0.750	Brouwer et al., 2020
COVA1-18	IGHV3-66	IGHJ4	IGLV7-46	IGLJ3	0.008	0.007	Brouwer et al., 2020
COVA1-21	IGHV3-30	IGHJ6	IGKV3-15	IGKJ2	0.040	0.160	Brouwer et al., 2020
COVA1-22	IGHV1-18	IGHJ6	IGLV3-1	IGLJ3	0.180	10.000	Brouwer et al., 2020
COVA1-25	IGHV4-39	IGHJ6	IGKV1-5	IGKJ3	0.180	10.000	Brouwer et al., 2020
COVA2-02	IGHV4-39	IGHJ6	IGKV1-39	IGKJ3	3.100	10.000	Brouwer et al., 2020

Table S1. Continued

COVA2-04	IGHV3-53	IGHJ6	IGKV3-20	IGKJ3	0.220	2.500	Brouwer et al., 2020
COVA2-05	IGHV5-51	IGHJ6	IGKV1-33	IGKJ4	5.700	10.000	Brouwer et al., 2020
COVA2-07	IGHV3-53	IGHJ6	IGKV3-20	IGKJ3	0.029	0.025	Brouwer et al., 2020
COVA2-11	IGHV1-69	IGHJ4	IGKV3-20	IGKJ4	3.700	10.000	Brouwer et al., 2020
COVA2-13	IGHV3-53	IGHJ6	IGKV3-20	IGKJ1	3.200	9.900	Brouwer et al., 2020
COVA2-15	IGHV3-23	IGHJ4	IGKV2-30	IGKJ2	0.008	0.009	Brouwer et al., 2020
COVA2-17	IGHV1-69	IGHJ4	IGKV3-11	IGKJ1	0.053	10.000	Brouwer et al., 2020
COVA2-20	IGHV3-53	IGHJ6	IGKV1-17	IGKJ1	0.730	1.500	Brouwer et al., 2020
COVA2-29	IGHV3-30	IGHJ3	IGKV1-39	IGKJ1	0.092	0.130	Brouwer et al., 2020
COVA2-37	IGHV1-24	IGHJ5	IGLV1-40	IGLJ3	4.000	10.000	Brouwer et al., 2020
COVA2-39	IGHV3-53	IGHJ3	IGLV2-23	IGLJ3	0.036	0.054	Brouwer et al., 2020
P2A-1A10	IGVH1-2	n.d.	IGKV2-40	n.d.	-	1.640	Ju et al., 2020
P2A-1A8	IGHV3-9	n.d.	IGLV2-14	n.d.	-	10.000	Ju et al., 2020
P2B-2F6	IGHV4-38-2	IGHJ3	IGLV2-8	IGLJ3	-	0.410	Ju et al., 2020
P2B-2G4	IGHV3-33	n.d.	IGLV2-11	n.d.	-	2.900	Ju et al., 2020
P2C-1A3	IGHV3-11	n.d.	IGKV1-9	n.d.	-	0.280	Ju et al., 2020
P2C-1C10	IGHV1-69	n.d.	IGKV3-11	n.d.	-	10.000	Ju et al., 2020
P2C-1F11	VH3-66	n.d.	IGKV3-20	n.d.	0.030	0.030	Ju et al., 2020
cov2-2130	IGHV3-15	IGHJ4	IGKV4-1	IGKJ4	-	0.186	Zost et al., 2020
cov2-2355	IGHV1-58	IGHJ3	IGKV3-20	IGKJ1	-	0.019	Zost et al., 2020
cov2-2504	IGHV1-2	IGHJ4	IGLV1-44	IGLJ2	-	0.015	Zost et al., 2020
cov2-2514	IGHV3-20	IGHJ3	IGLV3-19	IGLJ2	-	0.463	Zost et al., 2020
cov2-2678	IGHV3-20	IGHJ3	IGLV3-19	IGLJ3	-	0.264	Zost et al., 2020
cov2-2838	IGHV1-58	IGHJ3	IGKV3-20	IGKJ1	-	0.107	Zost et al., 2020
cov2-2952	IGHV3-66	IGHJ6	IGKV1-9	IGKJ5	-	0.363	Zost et al., 2020
CnC2t1p1 B10	IGHV1-69	IGHJ4	IGKV3-11	IGKJ4	-	10.000	Kreer et al., 2020
CnC2t1p1 B4	IGHV1-18	IGHJ5	IGLV2-23	IGLJ3	-	0.780	Kreer et al., 2020
CnC2t1p1 D6	IGHV3-49	IGHJ6	IGKV2-28	IGKJ3	-	3.720	Kreer et al., 2020
CnC2t1p1 E12	IGHV3-49	IGHJ6	IGKV2-28	IGKJ3	-	3.130	Kreer et al., 2020
CnC2t1p1 E8	IGHV1-2	IGHJ4	IGLV2-23	IGLJ3	-	4.420	Kreer et al., 2020
CnC2t1p1 G6	IGHV1-2	IGHJ4	IGLV2-23	IGLJ3	-	10.000	Kreer et al., 2020
FnC1t1p2 A5	IGHV1-8	IGHJ4	IGKV3-20	IGKJ1	-	10.000	Kreer et al., 2020
FnC1t2p1 D4	IGHV7-4-1	IGHJ5	IGKV1-33	IGKJ4	-	0.280	Kreer et al., 2020
FnC1t2p1 G5	IGHV7-4-1	IGHJ5	IGKV1-33	IGKJ4	-	0.330	Kreer et al., 2020
HbnC2t1p2 D9	IGHV3-33	IGHJ6	IGKV3-11	IGKJ1	-	0.930	Kreer et al., 2020
HbnC3t1p1 C6	IGHV1-58	IGHJ3	IGKV3-20	IGKJ1	-	0.040	Kreer et al., 2020
HbnC3t1p1 F4	IGHV3-30	IGHJ5	IGKV1-5	IGKJ4	-	0.780	Kreer et al., 2020
HbnC3t1p1 G4	IGHV3-66	IGHJ4	IGKV3-20	IGKJ1	-	0.120	Kreer et al., 2020
HbnC3t1p2_B1 0	IGHV3-66	IGHJ4	IGKV3-20	IGKJ2	-	0.250	Kreer et al., 2020
HbnC3t1p2 C6	IGHV1-58	IGHJ3	IGKV3-20	IGKJ1	-	0.330	Kreer et al., 2020
HbnC4t1p1 D5	IGHV3-9	IGHJ4	IGKV1-39	IGKJ4	-	10.000	Kreer et al., 2020
REGN10933	IGHV3-11	IGHJ4	IGKV1-33	IGKJ4	0.043	0.043	Hansen et al., 2020
REGN10934	IGHV3-15	IGHJ2	IGKV1-33	IGKJ1	0.054	0.054	Hansen et al., 2020
REGN10954	IGHV3-66	IGHJ4	IGKV1-33	IGKJ1	0.092	0.092	Hansen et al., 2020
REGN10964	IGHV4-4	IGHJ4	IGKV1-39	IGKJ3	0.057	0.057	Hansen et al., 2020
REGN10977	IGHV1-69	IGHJ4	IGKV3-20	IGKJ1	0.052	0.052	Hansen et al., 2020
REGN10984	IGHV3-66	IGHJ6	IGLV1-51	IGLJ3	0.097	0.097	Hansen et al., 2020
REGN10986	IGHV3-66	IGHJ4	IGLV1-40	IGLJ1	0.099	0.099	Hansen et al., 2020
REGN10987	IGHV3-30	IGHJ4	IGLV2-14	IGLJ3	0.041	0.041	Hansen et al., 2020
REGN10989	IGHV1-2	IGHJ5	IGLV2-14	IGLJ3	0.007	0.007	Hansen et al., 2020
S2M11	IGVH1-2	IGHJ4	IGKV3-20	IGKJ1	0.002	0.001	Tortorici et al. 2020
S2E12	IGVH1-58	IGHJ3	IGKV3-20	IGKJ1	0.002	0.004	Tortorici et al. 2020

Table S2. Cryo-EM data collection, refinement and validation statistics. Related to Figure 2.

	SARS-CoV-2 spike with Fab 2-43 (EMDB-23165) (PDB 7L56)	SARS-CoV-2 spike with Fab H4 (EMDB-23167) (PDB 7L58)	SARS-CoV-2 spike with Fab 2-15 (EMDB-23166) (PDB 7L57)
Data collection and processing			
Magnification	81,000	81,000	81,000
Voltage (kV)	300	300	300
Electron exposure (e ⁻ /Å ²)	51.69	42.00	52.40
Defocus range (μm)	-0.4 to -3.5	-0.5 to -3.5	-0.8 to -3.4
Pixel size (Å)	1.058	1.070	1.070
Symmetry imposed	C3	C1	C1
Initial particle images (no.)	199,753	1,070,123	882,010
Final particle images (no.)	61,434	102,290	16,590
Map resolution (Å)	3.60	5.07	5.87
FSC threshold	0.143	0.143	0.143
Refinement			
Initial model used (PDB code)	6XEY	6XEY	#### for xtal structure 6XEY
Map-to-model resolution (Å)	3.8	4.7	6.4
FSC threshold	0.5	0.5	0.5
Map sharpening <i>B</i> factor (Å ²)	-110.3	-121.2	-209.3
Model composition			
Non-hydrogen atoms	26,583	18103	17,415
Protein residues	3686	3442	3192
Ligands	67	41	54
<i>B</i> factors (Å²)			
Protein	77.79	142.43	232.59
Ligand	88.22	50.00	264.74
R.m.s. deviations			
Bond lengths (Å)	0.010	0.008	0.008
Bond angles (°)	1.094	1.340	1.287
Validation			
MolProbity score	1.27	1.57	1.73
Clashscore	0.98	1.89	2.57
Poor rotamers (%)	0.0	1.33	1.68
Ramachandran plot			
Favored (%)	92.14	90.74	91.22
Allowed (%)	7.86	8.99	8.62
Disallowed (%)	0.0	0.26	0.16

Table S3. Crystal structure data collection, refinement and validation statistics. Related to Figure 2.

SARS-CoV-2 RBD in complex with 2-15 Fab	
PDB ID	7L5B
<u>Data Collection</u>	
Space group	I 1 2 1
Unit cell dimensions	
<i>a,b,c</i> (Å)	134.013 70.439 140.039
α,β,γ (°)	90 96.932 90
Resolution range (Å)	102.49 - 3.182 (3.295 - 3.182)*
Total reflections	37768 (7212)
Unique reflections	20304 (2877)
Completeness (%)	93.26 (70.8)
Redundancy	2.7 (2.5)
$I/\sigma(I)$	12.80 (1.8)
R _{merge}	0.051 (0.630)
CC _{1/2}	0.989 (0.437)
<u>Refinement</u>	
Resolution range (Å)	102.49 - 3.182
Number of complexes per asymmetric unit	1
R _{work} /R _{free}	19.1/23.8
Number of atoms	
Protein	599
Ligands	0.0
B-factors	
Protein	64.10
RMS deviations	
Bond lengths (Å)	0.010
Bond angles (°)	1.41
Ramachandran statistics	
Favored (%)	86.37
Allowed (%)	13.63
Outliers (%)	0